


Stabilization of a transition state by excited vibration and impact on the reaction rate in the three-body Lennard-Jones system

Yoshiyuki Y. Yamaguchi ^{*}*Graduate School of Informatics, Kyoto University, Kyoto 606-8501, Japan*

(Received 4 September 2024; accepted 7 January 2025; published 11 February 2025)

The three-body Lennard-Jones system on the plane has a transition state, which is the straight conformation located at a saddle point of the potential-energy landscape. We show that the transition state can be dynamically stabilized by excited vibration of particle distances. The stabilization mechanism is explained theoretically and is verified by performing molecular dynamics simulations. We also examine whether the dynamical stabilization gives an impact on the reaction rate between the two isomers of equilateral triangle conformations by comparing with the transition-state theory.

DOI: [10.1103/PhysRevE.111.024204](https://doi.org/10.1103/PhysRevE.111.024204)

I. INTRODUCTION

The state is said to be unstable if the potential energy landscape takes a saddle or a local maximum at the corresponding state. A typical example is the inverted pendulum under the gravity. However, dynamics may change stability, and the inverted pendulum is stabilized by applying fast small oscillation of the pivot in the vertical direction. This pendulum is known as the Kapitza pendulum [1–4]. The essence of this dynamical stabilization is existence of multiple scales in time and space: The averaged fast small motion gives an additional term to the potential energy landscape, and the effective potential for slow motion may have a local minimum at the inverted position. Interestingly, the vertical motion of the pivot contributes to the stabilization in the orthogonal rotational direction.

The Kapitza pendulum is a nonautonomous system, but dynamical stabilization has been generalized to autonomous Hamiltonian systems [5,6]. Consider a chainlike model consisting of three beads and two springs, where two nearby beads are connected by a spring [7]. Comparing with the Kapitza pendulum, the two springs play the role of the oscillating pivot, and the angle between the two springs corresponds to the pendulum angle. Focusing on the angle motion, we can reduce the full system to a one-degree-of-freedom system, and the reduced part provides an additional potential, which may change the stability ruled by the bare potential energy landscape. This phenomenon is named by the dynamically induced conformation (DIC). It might be worth mentioning that vibration in the radial direction stabilizes the orthogonal rotational direction as the Kapitza pendulum.

DIC is firstly observed in numerical simulations of chainlike bead-spring systems [8], and is explained theoretically in three-body system [5] and later in N -body systems [6] by using the multiple-scale analysis [9] and the averaging method [10–12]. A remarkable difference of DIC from the Kapitza

pendulum is that the stabilization depends on excited modes of the vibration: The mode having the lowest eigenfrequency contributes to the stabilization, and contribution to the destabilization emerges by exciting higher eigenfrequency modes [5,6].

The previous studies on DIC have two restrictions: (i) the system should be chainlike and (ii) the bending potential which determines conformation is separately introduced in addition to the spring potential. Due to these restrictions, a system is out of range which has pairwise potentials but has no explicit bending potential, although such a system is important to study. For instance, the Lennard-Jones potential [13–15] is frequently used to model the intermolecular interaction.

In this article, we consider the three-body Lennard-Jones system on the plane, which is not a chainlike model but a ringlike model. The system has two minima, each of which corresponds to an equilateral triangle. Let the beads be named by A, B, and C. One triangle is ABC and the other is ACB. Due to two-dimensionality, between the two minima, there exists a transition state at which conformation is straight. The transition state is located at a saddle point of the potential energy landscape, but stabilization of the transition state is numerically observed and phenomenologically analyzed [16].

One of the aims of this article is to give a systematic explanation to the numerically observed stabilization by resulting in DIC. The other aim is to examine if DIC modifies the reaction rate, which is predicted by the transition state theory (TST) [17–24].

The three-body Lennard-Jones system on the plane is a simple model of isomerization, and it is a first step to deeply understand dynamical effects of isomerization in complex molecules. For example, excited mode dependence of isomer population has been examined experimentally [25,26]. Further, related dynamical effects have been observed in atomic clusters by considering the internal coordinates [27–30].

This paper is organized as follows. The three-body Lennard-Jones system is introduced and the potential energy landscape is analyzed in Sec. II. We show in Sec. III that the essence of DIC, separation of temporal and spatial scales, is

^{*}Contact author: yyama@amp.i.kyoto-u.ac.jp

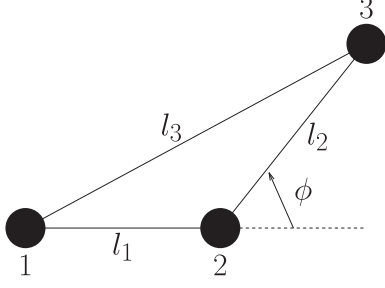


FIG. 1. Schematic figure of the three-body system with the definitions of l_1 , l_2 , l_3 , and ϕ .

realized intrinsically in the three-body Lennard-Jones system. Dynamically induced stability is studied in Sec. IV, and is examined in numerical simulations in Sec. V. The reaction rate is reported in Sec. VI. The last section VII is devoted to summary.

II. MODEL

We consider the three-body Lennard-Jones system on \mathbb{R}^2 . The system is described by the Lagrangian

$$L(\mathbf{r}, \dot{\mathbf{r}}) = \frac{1}{2} \sum_{i=1}^3 m \|\dot{\mathbf{r}}_i\|^2 - V(\mathbf{r}), \quad (1)$$

where $\mathbf{r}_i \in \mathbb{R}^2$ is the position of the i th mass, $\dot{\mathbf{r}}_i = d\mathbf{r}_i/dt$, $\|\cdot\|$ is the Euclidean norm, t is the time, and $\mathbf{r} = (\mathbf{r}_1, \mathbf{r}_2, \mathbf{r}_3)$. We assume that the three masses are identical. The total potential energy V consists of pairwise interactions as

$$V(\mathbf{r}) = U_{\text{LJ}}(l_1) + U_{\text{LJ}}(l_2) + U_{\text{LJ}}(l_3), \quad (2)$$

where

$$l_1 = \|\mathbf{r}_1 - \mathbf{r}_2\|, \quad l_2 = \|\mathbf{r}_2 - \mathbf{r}_3\|, \quad l_3 = \|\mathbf{r}_3 - \mathbf{r}_1\|. \quad (3)$$

A schematic figure of the system is shown in Fig. 1.

The pairwise potential U_{LJ} is the Lennard-Jones potential

$$U_{\text{LJ}}(l) = 4\epsilon_{\text{LJ}} \left[\left(\frac{\sigma}{l} \right)^{12} - \left(\frac{\sigma}{l} \right)^6 \right], \quad (4)$$

where σ and ϵ_{LJ} are real positive parameters. The equations of motion are

$$\frac{d^2 \mathbf{r}_i}{dt^2} = -\frac{4\epsilon_{\text{LJ}}}{m} \sum_{j=1}^3 \frac{\partial}{\partial \mathbf{r}_i} \left[\left(\frac{\sigma}{l_j} \right)^{12} - \left(\frac{\sigma}{l_j} \right)^6 \right], \quad (i = 1, 2, 3) \quad (5)$$

and the values of σ and ϵ_{LJ}/m are not essential, because we can set them as unity by rescaling the space \mathbf{r}_i and the time t . Landscape of the Lennard-Jones potential is illustrated in Fig. 2. It has the minimum value $U_{\text{LJ}}(l_{\min}) = -\epsilon_{\text{LJ}}$ at

$$l_{\min} = a_{\min} \sigma, \quad a_{\min} = 2^{1/6} = 1.122 \dots \quad (6)$$

A. Internal coordinates

The system has the translational symmetry and the rotational symmetry. The associated integrals are the total momentum vector and the total angular momentum. We set them as zero.

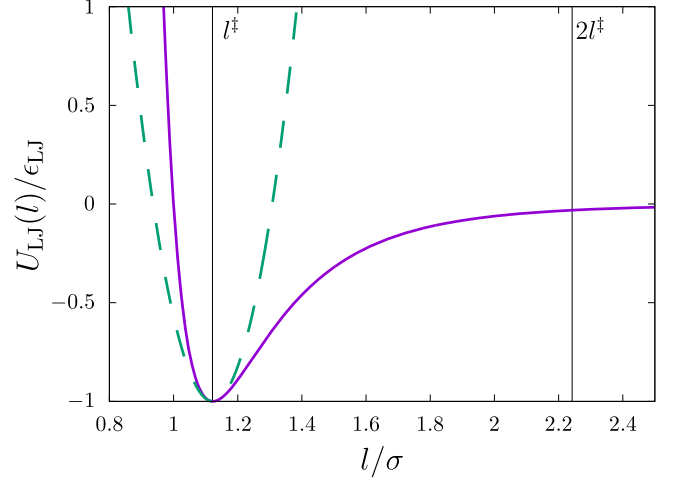


FIG. 2. Lennard-Jones potential (purple solid line). The lengths at a straight conformation are $l_1 = l_2 = l^*$ and $l_3 = 2l^*$, which are marked by the vertical black lines. The green broken curve represents the harmonic approximation around the bottom point.

We reduce the translational symmetry by introducing the internal coordinates $\mathbf{y} = (y_1, y_2, y_3, y_4) = (l_1, l_2, \phi, \phi_L)$. The angle ϕ is the bending angle between $\mathbf{r}_2 - \mathbf{r}_1$ and $\mathbf{r}_3 - \mathbf{r}_2$. For instance, $\phi = 0$ represents a straight conformation (see Fig. 1). The last angle variable ϕ_L is associated with the total angular momentum, which is another integral of the system.

The length l_3 is written as a function of (l_1, l_2, ϕ) as

$$l_3^2 = l_1^2 + l_2^2 + 2l_1 l_2 \cos \phi. \quad (7)$$

The total potential energy V is read as

$$V(\mathbf{y}) = U_{\text{LJ}}(l_1) + U_{\text{LJ}}(l_2) + U_{\text{LJ}}(\sqrt{l_1^2 + l_2^2 + 2l_1 l_2 \cos \phi}). \quad (8)$$

The Lagrangian in the internal coordinates is

$$L(\mathbf{y}, \dot{\mathbf{y}}) = \frac{1}{2} \sum_{\alpha, \beta=1}^4 B^{\alpha\beta}(\mathbf{y}) \dot{y}_\alpha \dot{y}_\beta - V(\mathbf{y}), \quad (9)$$

where $B^{\alpha\beta}(\mathbf{y})$ is the (α, β) element of the matrix $\mathbf{B}(\mathbf{y})$. See Appendix A for the explicit expression of $\mathbf{B}(\mathbf{y})$. The variable ϕ_L is not crucial since it is a cyclic coordinate associated with the rotational symmetry. Hereafter, we omit the angle ϕ_L , and use the same symbol \mathbf{y} for $\mathbf{y} = (y_1, y_2, y_3) = (l_1, l_2, \phi)$.

B. Stationary points of V

The potential V has two minima and three saddle points. The two minima are located at $(l_1, l_2, \phi) = (l_{\min}, l_{\min}, 2\pi/3)$ and $(l_{\min}, l_{\min}, -2\pi/3)$, which correspond to the equilateral triangle and the inverse equilateral triangle conformations. Between the two minima, there exists a saddle at $\mathbf{y}^\ddagger = (l^\ddagger, l^\ddagger, 0)$, which represents a straight conformation and which we focus on. We omit two other saddles (straight conformations) since they are obtained by changing the order of masses. The length l^\ddagger satisfies the stationarity condition

$$\frac{\partial V}{\partial l_i}(\mathbf{y}^\ddagger) = U'_{\text{LJ}}(l^\ddagger) + U'_{\text{LJ}}(2l^\ddagger) = 0, \quad i = 1, 2 \quad (10)$$

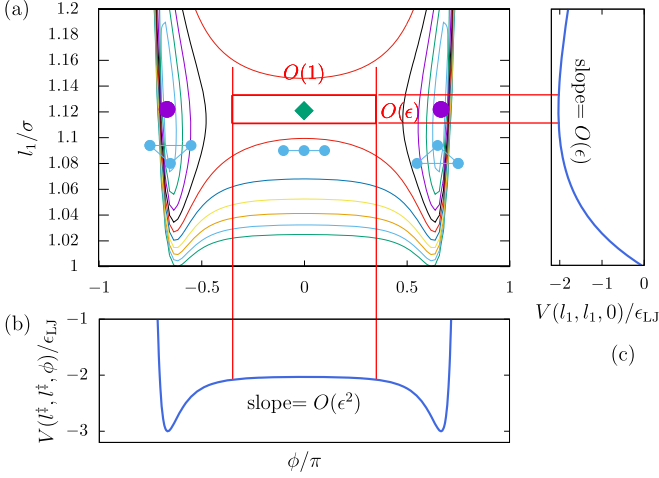


FIG. 3. Potential energy landscape of the three-body Lennard-Jones system on the section $l_2 = l_1$, i.e. $V(l_1, l_1, \phi)$. (a) Contours (curves), two minima (purple circles), and a saddle (green diamond). Conformations are presented by blue beads and lines. The red rectangle is the region in which we are interested. (b) Potential $V(l_1, l_1, \phi)/\epsilon_{\text{LJ}}$ as a function of ϕ . The slope is of $O(\epsilon^2)$ since $V(\mathbf{y}) - V(\mathbf{y}^\ddagger) = O(\epsilon^2)$ in the interested region. (c) Potential $V(l_1, l_1, 0)/\epsilon_{\text{LJ}}$ as a function of l_1 . The slope is of $O(\epsilon)$ in the interested region. See Eq. (17) for the definition of the small parameter ϵ .

since $l_3 = 2l^\ddagger$ at the saddle (see Fig. 2). The length l^\ddagger is

$$l^\ddagger = a\sigma, \quad a = \frac{1}{2} \left[\frac{2(2^{13} + 1)}{2^7 + 1} \right]^{1/6} = 1.121 \dots \quad (11)$$

We note that l^\ddagger is smaller than and close to l_{\min} . The values of $V(\mathbf{y})$ at the minima and the saddle are

$$\frac{V(l_{\min}, l_{\min}, \pm 2\pi/3)}{\epsilon_{\text{LJ}}} = -3, \quad \frac{V(\mathbf{y}^\ddagger)}{\epsilon_{\text{LJ}}} \simeq -2.031124. \quad (12)$$

The two minima and the saddle \mathbf{y}^\ddagger , which is a transition state, are illustrated in Fig. 3 with a contour map of $V(l_1, l_2, \phi)$ on the section $l_2 = l_1$. The straight conformation is unstable for the ϕ direction with respect to the bare potential V , the conformation can be stabilized by fast vibration of l_1 and l_2 however: This is DIC.

III. MULTISCALE ANALYSIS

The essential mechanism of DIC is separation of temporal and spatial scales. In the previous studies [5,6], to realize slow bending motion of ϕ , the total potential is composed of the spring potential $V_{\text{spring}}(l_1, l_2)$ and the bending potential $\epsilon^2 V_{\text{bend}}(\phi)$, where ϵ is a small dimensionless parameter ϵ ($0 < \epsilon \ll 1$). We demonstrate that the three-body Lennard-Jones system induces, intrinsically, the separation of scales and a bending potential of $O(\epsilon^2)$ around the transition state \mathbf{y}^\ddagger .

A. Separation of timescales

We estimate the timescales around the transition state \mathbf{y}^\ddagger by considering the linearized equations of motion. The Taylor expansion of the total potential V around \mathbf{y}^\ddagger gives

$$\nabla V(\mathbf{y}) = H_V(\mathbf{y}^\ddagger)(\mathbf{y} - \mathbf{y}^\ddagger) + \dots, \quad (13)$$

where

$$H_V(\mathbf{y}^\ddagger) = U''_{\text{LJ}}(l^\ddagger) \begin{pmatrix} 1 & 0 & 0 \\ 0 & 1 & 0 \\ 0 & 0 & 0 \end{pmatrix} + U''_{\text{LJ}}(2l^\ddagger) \begin{pmatrix} 1 & 1 & 0 \\ 1 & 1 & 0 \\ 0 & 0 & 0 \end{pmatrix} - \frac{U'_{\text{LJ}}(2l^\ddagger)}{2l^\ddagger} (l^\ddagger)^2 \begin{pmatrix} 0 & 0 & 0 \\ 0 & 0 & 0 \\ 0 & 0 & 1 \end{pmatrix} \quad (14)$$

is the Hessian of V at $\mathbf{y} = \mathbf{y}^\ddagger$.

The Hessian matrix implies that the timescale τ_l of l_i is determined by the first and the second terms of H_V , and that the timescale τ_ϕ of ϕ by the third term. In the third term we extracted $(l^\ddagger)^2$ to adjust the physical dimension. The coefficients are estimated as

$$\begin{aligned} U''_{\text{LJ}}(l^\ddagger) &= \frac{24\epsilon_{\text{LJ}}}{a^{12}(l^\ddagger)^2} (26 - 7a^6) \simeq \frac{24\epsilon_{\text{LJ}}}{a^{12}(l^\ddagger)^2} 12.1068, \\ U''_{\text{LJ}}(2l^\ddagger) &= \frac{24\epsilon_{\text{LJ}}}{a^{12}(l^\ddagger)^2} \frac{26 - 7(2a)^6}{2^{14}} \simeq \frac{24\epsilon_{\text{LJ}}}{a^{12}(l^\ddagger)^2} (-0.05268), \\ \frac{U'_{\text{LJ}}(2l^\ddagger)}{2l^\ddagger} &= -\frac{24\epsilon_{\text{LJ}}}{a^{12}(l^\ddagger)^2} \frac{2 - (2a)^6}{2^{14}} \simeq \frac{24\epsilon_{\text{LJ}}}{a^{12}(l^\ddagger)^2} 0.00763. \end{aligned} \quad (15)$$

The first term $U''_{\text{LJ}}(l^\ddagger)$ dominates the second term $U''_{\text{LJ}}(2l^\ddagger)$, and the timescales are estimated as

$$\tau_l = \sqrt{\frac{m}{U''_{\text{LJ}}(l^\ddagger)}}, \quad \tau_\phi = \sqrt{\frac{m}{U'_{\text{LJ}}(2l^\ddagger)/(2l^\ddagger)}}. \quad (16)$$

Separation of the two timescales is now clear and we introduce a small dimensionless parameter ϵ as

$$\epsilon = \frac{\tau_l}{\tau_\phi} = \sqrt{\frac{U'_{\text{LJ}}(2l^\ddagger)/(2l^\ddagger)}{U''_{\text{LJ}}(l^\ddagger)}} \simeq 0.0251. \quad (17)$$

The small parameter ϵ introduces multiple timescales: the fast timescale $t_0 = t$ corresponding to τ_l and the slow timescale $t_1 = \epsilon t$ corresponding to τ_ϕ . We consider that t_0 and t_1 are independent variables. The time derivative is expanded as

$$\frac{d}{dt} = \frac{\partial}{\partial t_0} + \epsilon \frac{\partial}{\partial t_1}. \quad (18)$$

B. Spatial scale and potential forces

For the dependent variables, we are interested in a region close to the transition state \mathbf{y}^\ddagger and, from Fig. 3, we expand them as

$$l_i(t_0, t_1) = l^\ddagger + \epsilon l_i^{(1)}(t_0, t_1), \quad i = 1, 2 \quad (19a)$$

$$\phi(t_0, t_1) = \phi^{(0)}(t_1) + \epsilon \phi^{(1)}(t_0, t_1), \quad (19b)$$

which is simply denoted by

$$\mathbf{y}(t_0, t_1) = \mathbf{y}^{(0)}(t_1) + \epsilon \mathbf{y}^{(1)}(t_0, t_1). \quad (20)$$

Smallness of $|\epsilon l_i^{(1)}|$ is realized by selecting suitable initial conditions.

We consider the potential force again, which is expanded as

$$\nabla V(\mathbf{y}) = \epsilon(\nabla V(\mathbf{y}))^{(1)} + \epsilon^2(\nabla V(\mathbf{y}))^{(2)} + \dots, \quad (21)$$

where, for an arbitrary function $A(\mathbf{y})$, $(A(\mathbf{y}))^{(n)}$ represents the $O(\epsilon^n)$ part of $A(\mathbf{y})$. From Eqs. (13), (14), and (17), we have

$$(\nabla V(\mathbf{y}))^{(1)} = U_{\text{LJ}}''(l^\ddagger) \begin{pmatrix} l_1^{(1)} \\ l_2^{(1)} \\ 0 \end{pmatrix} \quad (22)$$

and

$$(\nabla V(\mathbf{y}))^{(2)} = -U_{\text{LJ}}''(l^\ddagger)(l^\ddagger)^2 \begin{pmatrix} * \\ * \\ \phi \end{pmatrix}. \quad (23)$$

The asterisk parts are not important in the later discussions and we neglect them. The bending potential depending on ϕ appears from $O(\epsilon^2)$ without any artificial scalings. The two scales of ∇V can be understood graphically in Fig. 3 with the fact $V(\mathbf{y}) - V(\mathbf{y}^\ddagger) = O(\epsilon^2)$ around \mathbf{y}^\ddagger .

C. Universality

The expansions (18), (19), and (22) are the same as ones used in the previous analyses [5,6], whereas the three-body Lennard-Jones system does not satisfy the two restrictions mentioned in Sec. I. Therefore, DIC should be reproduced around the transition state \mathbf{y}^\ddagger .

Let us revisit the origin of the above expansions. The two timescales and $(\partial V/\partial \phi)^{(1)} = 0$ are induced from smallness of the ratio (17). Thus, we may expect emergence of DIC in other systems apart from the Lennard-Jones potential, if the pairwise potential U has a steep well [i.e. large $U''(l^\ddagger)$] and a gradual tail [i.e. small $U'(2l^\ddagger)/(2l^\ddagger)$]. A harmonic potential $U(l) = k(l - \sigma)^2/2$ is out of this scope, since $U''(l^\ddagger) = U''(2l^\ddagger) = k$ and $U'(2l^\ddagger)/(2l^\ddagger) = k/4$ are of the same order, where the stationary length l^\ddagger satisfying Eq. (10) is $l^\ddagger = 2\sigma/3$.

IV. DYNAMICAL STABILITY OF THE TRANSITION STATE

Along computations performed in [5,6], we can reduce the three-dimensional dynamical system of (l_1, l_2, ϕ) to the one-dimensional dynamical system of $\phi^{(0)}(t_1)$, which appears in $O(\epsilon^2)$. We sketch the derivation. See Appendix B for details.

In $O(\epsilon)$, we have linear equations of motion for fast motion of $l_1^{(1)}$ and $l_2^{(1)}$. The two lengths l_1 and l_2 extend and contract simultaneously in the in-phase mode (mode-I) and alternatively in the antiphase mode (mode-II). If we modify l_1 and l_2 initially from the equilibrium value l^\ddagger as

$$l_i = l^\ddagger + \delta l_i, \quad (i = 1, 2), \quad (24)$$

the initial values of the mode-I energy E_I and the mode-II energy E_{II} are

$$E_I = \frac{U_{\text{LJ}}''(l^\ddagger)}{4}(\delta l_1 + \delta l_2)^2, \quad E_{II} = \frac{U_{\text{LJ}}''(l^\ddagger)}{4}(\delta l_1 - \delta l_2)^2. \quad (25)$$

We hypothesize that the ratio between the two normal-mode energy E_I and E_{II} is constant in time [5,6], and introduce $\nu_I : \nu_{II} = E_I : E_{II}$ with $\nu_I + \nu_{II} = 1$.

The equation of motion for $\phi^{(0)}(t_1)$ is obtained in $O(\epsilon^2)$, which includes the fast motion of $l_1^{(1)}(t_0, t_1)$ and $l_2^{(1)}(t_0, t_1)$. Performing the averaging over the fast timescale t_0 , we can eliminate the initial phases of the two normal modes, but cannot eliminate the energy ratios, ν_I and ν_{II} . This is the origin of the excited mode dependence in DIC.

The above-mentioned averaging induces an extra force to $\phi^{(0)}(t_1)$ in addition to the potential gradient. The effective force F_{eff} of $O(\epsilon^0)$ to the slow motion of $\phi^{(0)}(t_1)$ is expressed as

$$\epsilon^2 F_{\text{eff}}(\phi^{(0)}) = -\frac{\partial V}{\partial \phi}(l^\ddagger, l^\ddagger, \phi^{(0)}) - \frac{E_{\text{normal}}}{2} T(\phi^{(0)}). \quad (26)$$

We remark that the potential force $\partial V/\partial \phi$ in Eq. (26) is of $O(\epsilon^2)$ from Eqs. (22) and (23), and $E_{\text{normal}} = E_I + E_{II}$ is also of $O(\epsilon^2)$ from (25). The function $T(\phi^{(0)})$ is defined by

$$T(\phi^{(0)}) = \sin \phi^{(0)} \left(\frac{\nu_I}{2 - \cos \phi^{(0)}} - \frac{\nu_{II}}{2 + \cos \phi^{(0)}} \right). \quad (27)$$

Integrating the effective force (26), we have the effective potential $V_{\text{eff}}(\phi)$ for the angle ϕ as

$$V_{\text{eff}}(\phi) = V(l^\ddagger, l^\ddagger, \phi) + \frac{E_{\text{normal}}}{2} [\nu_I \log(2 - \cos \phi) + \nu_{II} \log(2 + \cos \phi)]. \quad (28)$$

Examples of the effective potential V_{eff} are shown in Fig. 4. The in-phase mode stabilizes the straight conformation $\phi = 0$, while the antiphase mode enhances instability. This mode dependence is the same as the chainlike model [5,6]. The bare potential V is of $O(\epsilon^0)$ and E_{normal} is of $O(\epsilon^2)$, the additional potential function is visible however for $|\delta l|/\sigma \simeq 0.05$, since $U_{\text{LJ}}''(l^\ddagger)/4$ appearing in (25) gives a factor

$$\frac{U_{\text{LJ}}''(l^\ddagger)}{4} \simeq \frac{\epsilon_{\text{LJ}}}{\sigma^2} 14.6737 \quad (29)$$

and $E_{\text{normal}}/\epsilon_{\text{LJ}}$ is around 0.15.

We remark an important modification from the previous work [5]. In the previous work, the normal mode energy E_{normal} is eliminated in the effective potential $V_{\text{eff}}(\phi)$ by using the total energy conservation, which includes energy of $\phi^{(0)}$ motion. The total energy conservation provides a global effective potential under the hypothesis that the ratio $\nu_I : \nu_{II}$ is constant of time globally. In other words, the obtained effective potential is valid for any value of ϕ . The constant ratio hypothesis is not bad in a chainlike model, but it is not good in the three-body Lennard-Jones system if ϕ is far from 0, because thermalization occurs easily (see Sec. V D for a numerical test and Sec. VI for a success of a statistical theory). Therefore, we concentrate on a neighborhood of $\phi = 0$ in which the hypothesis should be valid, and the effective potential (28) is valid only around $\phi = 0$.

Stability of the transition state $\mathbf{y}^\ddagger = (l^\ddagger, l^\ddagger, 0)$ is determined by the signature of

$$V_{\text{eff}}''(0) = \frac{\partial^2 V}{\partial \phi^2}(\mathbf{y}^\ddagger) + \frac{3\nu_I - \nu_{II}}{6} E_{\text{normal}}. \quad (30)$$

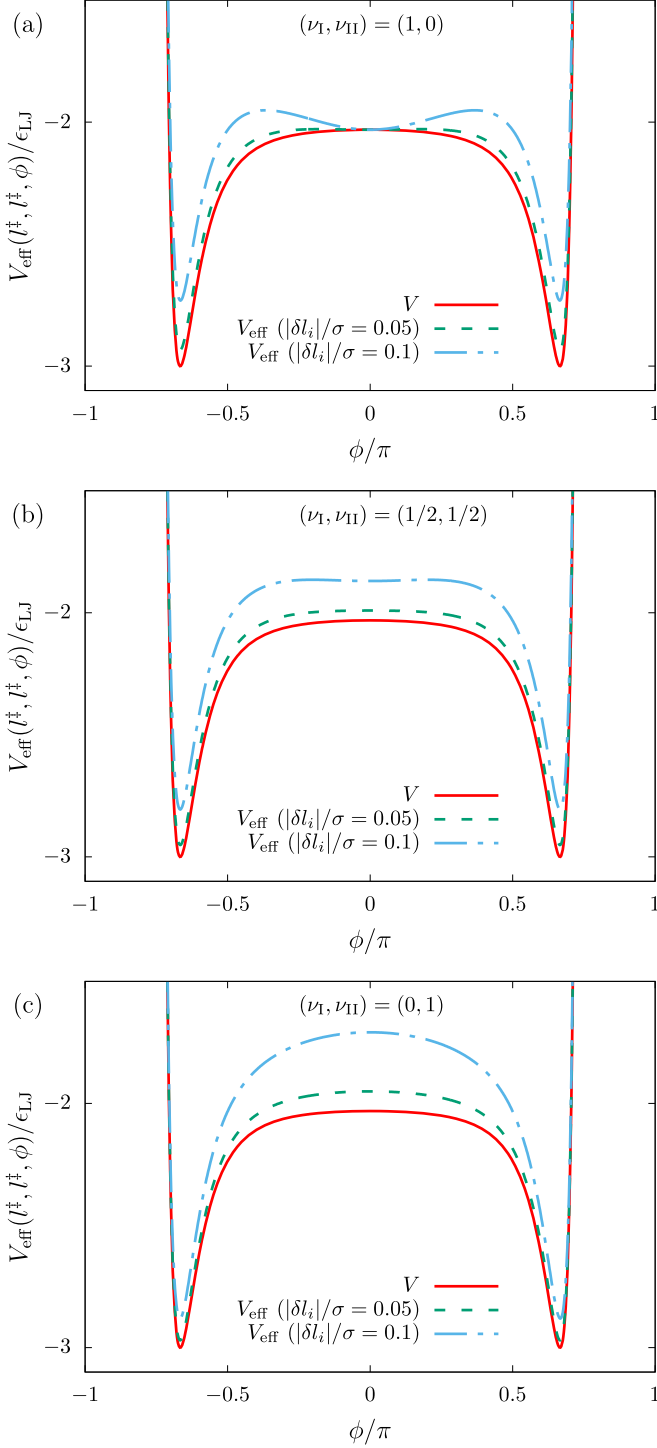


FIG. 4. Effective potential $V_{\text{eff}}(\phi)$. Bare potential V (red solid), effective potential V_{eff} with $|\delta l_1|/\sigma = |\delta l_2|/\sigma = 0.05$ (green broken), and 0.1 (blue dot-dashed). (a) In-phase mode $(\nu_I, \nu_{II}) = (1, 0)$. (b) Equally mixed mode $(\nu_I, \nu_{II}) = (1/2, 1/2)$. (c) Antiphase mode $(\nu_I, \nu_{II}) = (0, 1)$.

It is clear that the in-phase mode (mode-I) contributes to stabilization, and that the antiphase mode (mode-II) to destabilization. Using Eqs. (2), (7), and (25), we modify $V_{\text{eff}}''(0)$ as

$$V_{\text{eff}}''(0) = \frac{\sigma^2}{12} U_{\text{LJ}}''(l^{\ddagger}) S, \quad (31)$$

where

$$S = -12\epsilon^2 a^2 + \frac{\delta l_1^2 + \delta l_2^2 + 4\delta l_1 \delta l_2}{\sigma^2} \quad (32)$$

plays the role of the stability index: $S > 0$ ($S < 0$) means stable (unstable) since $U_{\text{LJ}}''(l^{\ddagger}) > 0$. The constant term is

$$12\epsilon^2 a^2 \simeq 0.0095. \quad (33)$$

V. MOLECULAR DYNAMICS SIMULATIONS

We examine the theoretical stability $S > 0$ [see Eq. (32)] by comparing it with molecular dynamics (MD) simulations. We set $m = 1$, $\sigma = 1$, and $\epsilon_{\text{LJ}} = 1$ without loss of generality by rescaling the time t and space \mathbf{r}_i in the equations of motion (5), although we keep the symbols to clarify the source. MD simulations are performed by using the 4th order symplectic integrator [31] with the timestep $\Delta t = 10^{-3}$ to keep the symplectic structure and to realize high precision.

A. Initial condition

The initial velocities of particles are zero, $\dot{\mathbf{r}}_i = \mathbf{0}$ ($i = 1, 2, 3$), and the initial momenta are zero accordingly. The initial positions are shifted from the saddle point as

$$\begin{pmatrix} x_1(0) \\ x_2(0) \\ x_3(0) \end{pmatrix} = \begin{pmatrix} -l^{\ddagger} + \delta x_1 \\ -\delta x_1 - \delta x_3 \\ l^{\ddagger} + \delta x_3 \end{pmatrix}, \quad \begin{pmatrix} y_1(0) \\ y_2(0) \\ y_3(0) \end{pmatrix} = \begin{pmatrix} -\delta y/2 \\ \delta y \\ -\delta y/2 \end{pmatrix}. \quad (34)$$

The displacements δx_1 and δx_3 are transformed to δl_i as

$$\delta l_1 = -2\delta x_1 - \delta x_3, \quad \delta l_2 = \delta x_1 + 2\delta x_3, \quad (35)$$

and we vary $\delta l_1/\sigma$ and $\delta l_2/\sigma$. $\delta y = 10^{-3}$ is given as a perturbation to modify the value of ϕ from zero. If $\delta l_1 = \delta l_2 = \delta y = 0$, the state is exactly at the transition state and no temporal evolution occurs.

B. Temporal evolution

First, we observe temporal evolution of l_3/l^{\ddagger} , shown in Fig. 5. The quantity l_3/l^{\ddagger} is close to 2 if the system stays around the straight conformation (a transition state), and is close to 1 if the system is around an equilateral triangle conformation (a minimum). In other words, $l_3/l^{\ddagger} \simeq 2$ implies stabilization of the transition state, and $l_3/l^{\ddagger} \simeq 1$ implies non-stabilization.

The initial excitation of the normal modes is controlled by the signs of δl_i : $E_I > E_{II}$ if the signs are the same, and $E_I < E_{II}$ if the signs are opposite. In Figs. 5(a) and 5(d), the antiphase mode (mode-II) is dominant as $E_I/E_{II} = 1/9$, and the straight conformation is not stabilized. However, in Figs. 5(b) and 5(c), the in-phase mode (mode-I) is dominant as $E_I/E_{II} = 9$, and the straight conformation is stabilized up to $t \simeq 600$ at least. Temporal evolution of l_3/l^{\ddagger} is consistent with the effective potential shown in Fig. 4. To clarify a qualitative difference of dynamics between a nonstabilized saddle and a stabilized one, power spectra of $l_1(t)$ are reported in Appendix C.

Asymmetry between Figs. 5(b) and 5(c) is explained as follows. The Lennard-Jones potential has a steeper wall in

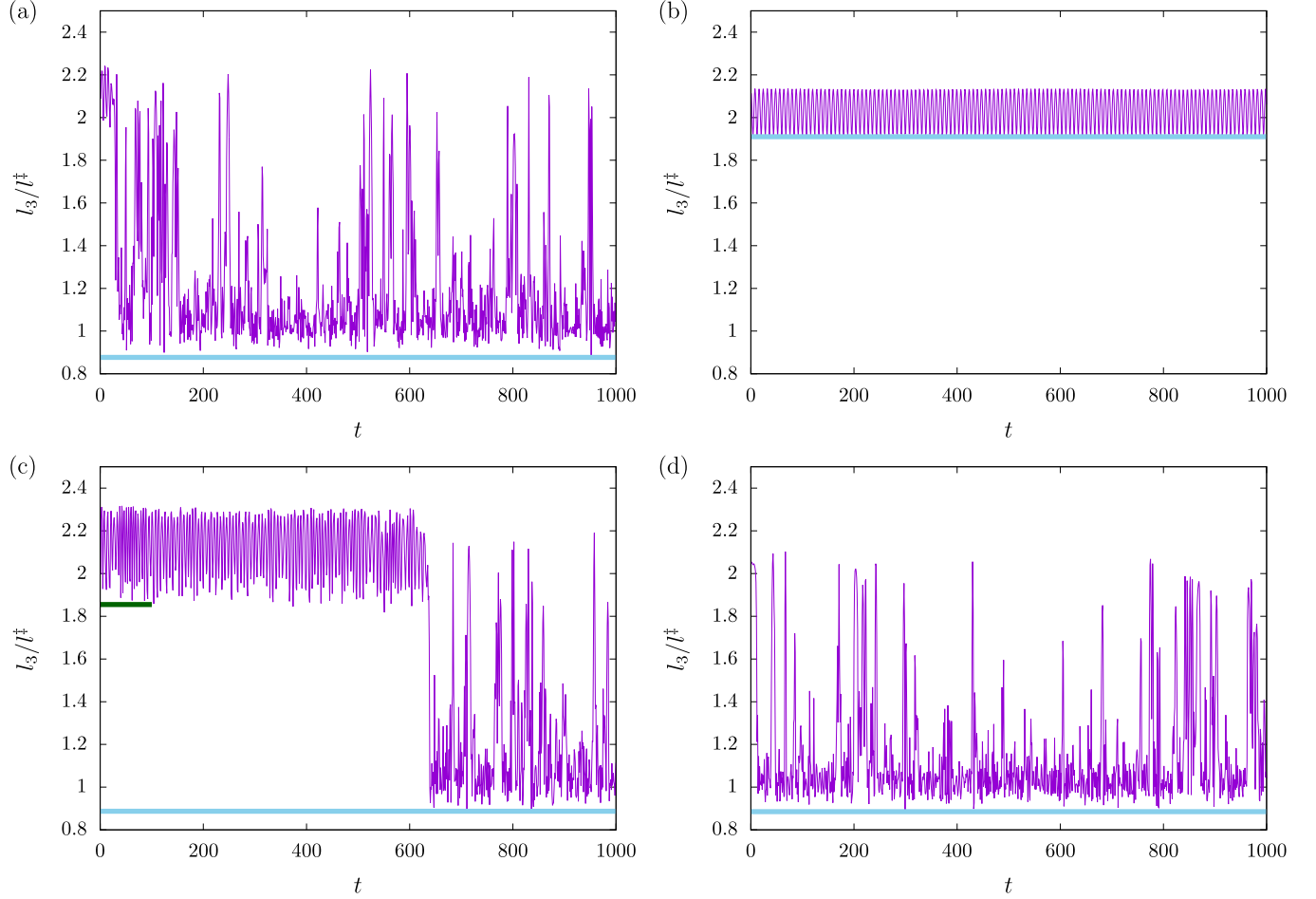


FIG. 5. Temporal evolution of l_3/l^* . $(\delta l_1/\sigma, \delta l_2/\sigma)$ is (a) $(-0.1, 0.05)$, (b) $(0.1, 0.05)$, (c) $(-0.1, -0.05)$, and (d) $(0.1, -0.05)$. The blue horizontal line represents $l_{3,\min}(10^3)$, and the green short horizontal line represents $l_{3,\min}(10^2)$ in (c) [see Eq. (36) for $l_{3,\min}(T)$]. The theoretical stability index S is $S = -0.017$ for (a) and (d), and $S = 0.023$ for (b) and (c).

the contracting direction $\delta l_i < 0$ than the extending direction $\delta l_i > 0$ as shown in Fig. 2. Nonlinear effects are hence stronger in Fig. 5(c) than in Fig. 5(b), while the theory cannot capture them since it approximates E_{normal} by a harmonic potential. See also the green broken curve in Fig. 2.

C. Stability diagram

Stability is explored at each sample point on the plane $(\delta l_1/\sigma, \delta l_2/\sigma)$ by computing

$$\tilde{l}_{3,\min}(T) = \min_{t \in [0, T]} \frac{l_3(t)}{l^*}. \quad (36)$$

We set $T = 10^2$ and $T = 10^3$ in Figs. 6(a) and 6(b) respectively. The theoretical prediction by the index S is shown in Fig. 6(c). Numerical observation is almost in good agreement with the theoretical prediction. The in-phase (antiphase) mode axis runs from the left-lower (right-lower) corner to the right-upper (left-upper) corner. Excitation of the in-phase mode stabilizes the straight conformation if the excitation is sufficiently strong, as we have observed in previous works [5,6].

Slight discrepancies between numerical observation and the theoretical prediction observed along the in-phase mode

axis in particular is again explained by asymmetry of the Lennard-Jones potential in the contracting and extending directions. Indeed, the total energy is asymmetric [see Fig. 6(d)]. E_{normal} is underestimated in the contracting direction, while it is overestimated in the extending direction. The theoretical underestimation (overestimation) induces that numerical simulations gain (lose) stability around the boundary of stability.

The same analysis is performed in Fig. 7 for a wider range of δl_1 and δl_2 . A larger $|\delta l_i|$ gives a large value of the total energy and induces frequent evaporation. Nevertheless, DIC emerges in a upper-right region in particular. Validity of the expansion, Eq. (19a), is no longer guaranteed in such a wider range, but stabilization of the transition state is captured in a short time regime except for the evaporation.

D. Test of hypothesis

We close this section by performing a numerical test of the hypothesis: The ratio $v_I : v_{II}$ is constant of time. The initial condition is $(\delta l_1, \delta l_2) = (-0.07, -0.08)$, which gives stability of the transition state only in a short term (see Fig. 6).

The expressions of E_I and E_{II} [see Eqs. (B19) and (B20)] are derived by the harmonic approximation, but this approximation is not excellent if $|\delta l_1|$ and $|\delta l_2|$ are large (see Fig. 2).

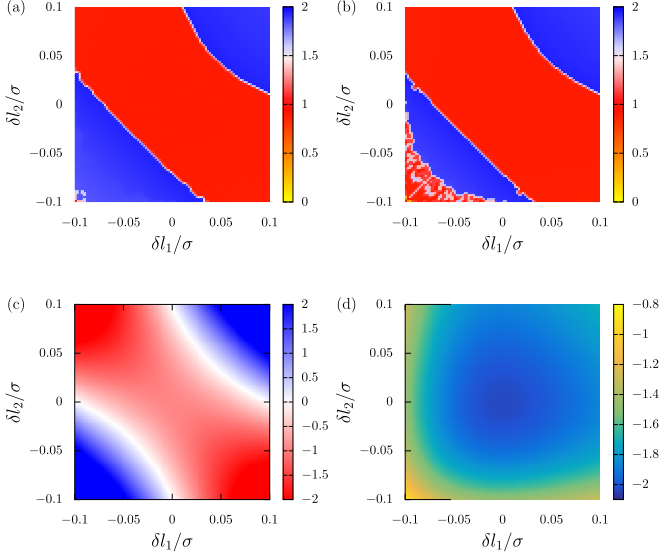


FIG. 6. Stability of the transition state. (a) $\tilde{l}_{3,\min}(T = 10^2)$. (b) $\tilde{l}_{3,\min}(T = 10^3)$. Note $\tilde{l}_{3,\min} \simeq 2$ ($\tilde{l}_{3,\min} \simeq 1$) implies that the transition state is (is not) stabilized. In (a) and (b) the color bar starts from 0, where 0 is assigned to evaporation of a particle. (c) Theoretical stability index $S \times 10^2$. Color bar range is truncated. $S > 0$ predicts emergence of DIC (dynamical stabilization). (d) Total energy.

We then compute ν_I and ν_{II} as time averages of relative amplitudes $[l_1^{(1)} + l_2^{(1)}]^2$ and $[l_1^{(1)} - l_2^{(1)}]^2$ respectively. The averages are taken in each time window of length 5. For instance, the n th point of ν_I , denoted by $\nu_I(n)$, is defined by

$$\nu_I(n) = \frac{1}{5} \int_{5n}^{5(n+1)} [l_1(t) + l_2(t) - 2l^\ddagger]^2 dt. \quad (37)$$

Temporal evolution of ν_I and ν_{II} is reported in Fig. 8 with temporal evolution of ϕ . They are almost constant when $\phi \simeq 0$, and go away after $t \simeq 800$, at which the system moves

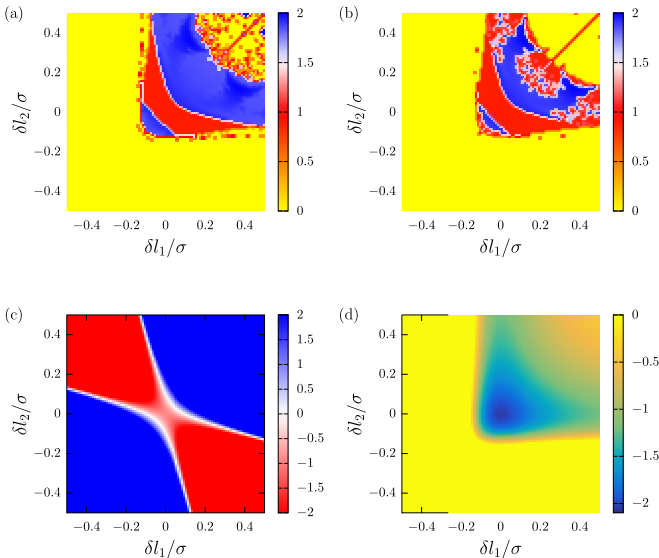


FIG. 7. Same as Fig. 6, but in a wider region of $(\delta l_1/\sigma, \delta l_2/\sigma)$. In panels (a) and (b), evaporation occurs at points where the color bar is 0 (yellow). Color bar range is truncated in all panels.

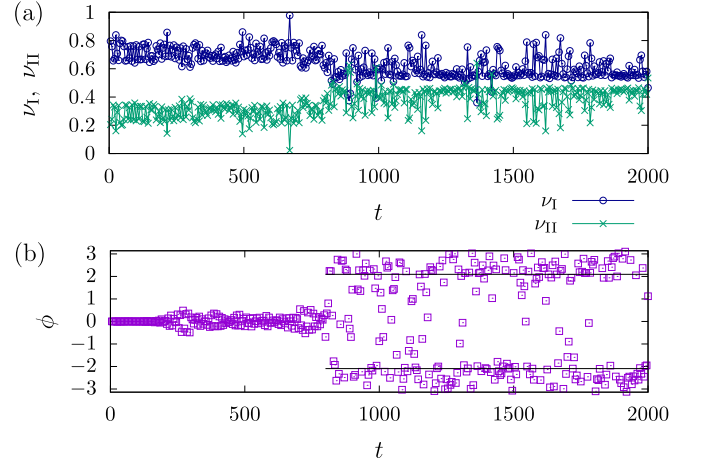


FIG. 8. Hypothesis test. The initial condition is $(\delta l_1, \delta l_2) = (-0.07, -0.08)$. (a) Averaged temporal evolution of ν_I (blue circles) and ν_{II} (green crosses). (b) Temporal evolution of ϕ . Two horizontal black lines mark $\pm 2\pi/3$ corresponding to the equilateral triangles.

away from the transition state. We hence conclude that the hypothesis is valid while stabilization of the transition state is realized.

VI. REACTION RATE

The transition state can be stabilized by the fast motion of l_1 and l_2 . The next question is whether the stabilization changes the reaction rate statistically. To answer this question, we compute the reaction rate by TST and MD simulations. The reaction rate is defined as the decrease in reactant (the increase in product) per unit time.

TST is a theory to explain the reaction rate by using statistical mechanics. The idea of TST is as follows. We introduce a dividing surface that divides the reactant and the product in the phase space. Then, we compute the ratio between two phase volumes: the volume which passes the dividing surface within the unit time, and the phase volume of the reactant.

A more precise explanation is as follows. Let the three bodies be A, B, and C. In our setting, the reactant is, for instance, the triangle ABC, and the product is the triangle ACB. Let us denote the Hamiltonian of the system by $H(\mathbf{y}, \mathbf{p})$. TST gives an expression of the reaction rate $k(E)$ for total energy E by

$$k(E) = \frac{3 \int_{\dot{\phi} > 0} \delta(E - H(\mathbf{y}, \mathbf{p})) \delta(\phi) \dot{\phi} d\mathbf{y} d\mathbf{p}}{\frac{1}{2} \int \delta(E - H(\mathbf{y}, \mathbf{p})) d\mathbf{y} d\mathbf{p}}. \quad (38)$$

For the reaction route which passes the transition state $\mathbf{y}^\ddagger = (l^\ddagger, l^\ddagger, 0)$, we may set the dividing surface as $\phi = 0$, and the numerator represents the flux passing the dividing surface in the unit time from one side to the other. The factor 3 counts the three routes of isomerization associated with the three transition states. The denominator is the half of the phase space volume for total energy E , which corresponds to the phase space volume of the reactant by symmetry. Concrete expressions of $H(\mathbf{y}, \mathbf{p})$, momenta $\mathbf{p} = (p^1, p^2, p^3)$, and $\dot{\phi}$ are reported in Appendix D. Recall that the total angular momentum is set as zero.

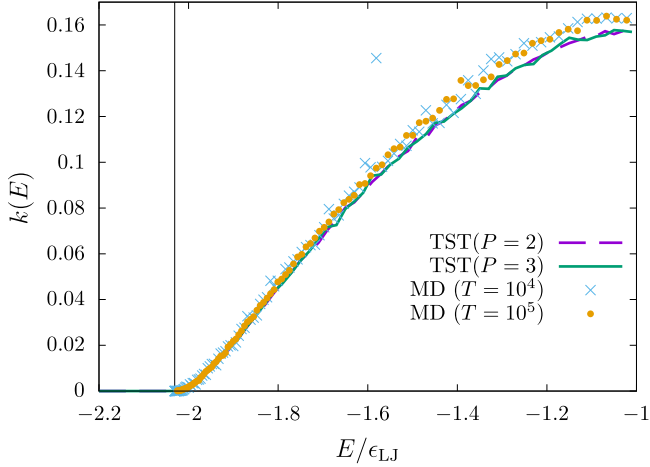


FIG. 9. Reaction rate $k(E)$ as a function of E/ϵ_{LJ} , where E is the total energy. The lines represent the transition state theory with $P = 2$ (purple broken) and $P = 3$ (green solid). Points are from direct molecular dynamics simulations with $T = 10^4$ (blue crosses) and $T = 10^5$ (orange circles). The vertical line marks the total potential energy at the transition state, $V(\mathbf{y}^\ddagger)/\epsilon_{\text{LJ}} \simeq -2.03$.

To compute $k(E)$ of Eq. (38) numerically, we truncate the phase space as $l_1, l_2 \in [0.8, 3]$, $\phi = [0, 2\pi)$, $p^1, p^2, p^3 \in [-P, P]$. We examine $P = 2$ and $P = 3$ to confirm that $P = 3$ is sufficiently large. On each truncated axis 100 points are equally distributed, and the value of $H(\mathbf{y}, \mathbf{p})$ and the weight ϕ are computed totally at 10^{12} points. Finally, we make a histogram with respect to E by dividing the interval $E \in [-3, -1]$ into 100 bins, where the representative point of the i th bin is $E_i = -3 + 2(i + 0.5)/100$ ($i = 0, \dots, 99$). We neglected $E > -1$ since a particle may evaporate.

The reaction rate $k(E)$ is also computed by following the definition and performing direct MD simulations. The initial condition is the one introduced in Sec. V A with the constraint $\delta l_2 = -\delta l_1$ to make the transition state unstable. The total energy E depends on δl_1 . The reaction rate $k(E)$ is obtained as $k(E) = N(E, T)/T$, where $N(E, T)$ is the number of isomerization during the time interval $t \in [0, T]$, and we set the computing time T as $T = 10^4$ and $T = 10^5$. We remark that this reaction rate counts isomerizations from ABC to ACB and from ACB to ABC, while Eq. (38) considers only from ABC to ACB. We can define a corresponding reaction rate in dynamics by discarding the periods in which the system is in the well of ACB. However, this modification reduces T and $N(E, T)$ by half from symmetry, and we keep all the periods to enrich statistics.

The reaction rate $k(E)$ is reported in Fig. 9. First, we confirm that $P = 3$ is sufficiently large for obtaining the theoretical precision, since the line with $P = 3$ collapses on the line with $P = 2$. Second, by a similar reason, $T = 10^5$ is sufficiently large for obtaining the reaction rate by MD simulations. Therefore, we conclude that the theoretical prediction slightly underestimates the dynamical result for $-1.6 \lesssim E < -1$. However, the theoretical prediction is not far from MD, and the dynamical stabilization does not strongly affect the reaction rate in the three-body Lennard-Jones system irrespective of emergence of dynamical (de)stabilization.

VII. SUMMARY

Dynamically induced conformation (DIC) is a stabilization mechanism of an unstable conformation with respect to a bare potential energy landscape, and it is an analogy of the Kapitza pendulum in autonomous systems. DIC has been previously studied in chainlike bead-spring models with an artificially induced weak bending potential function [5,6]. This article demonstrated that in the three-body Lennard-Jones potential, the transition state (a straight conformation) is also dynamically stabilized, although the system is neither a chainlike system nor introducing any artificial potential. DIC in the three-body Lennard-Jones system is based on the fact that the potential has a steep well and a gradual tail, and we may expect emergence of DIC in a similar system, while a system with a harmonic pairwise potential is out of the range of the present theory.

We can derive an effective potential, which is the sum of the bare potential and the dynamical effect in the direction of conformation change. The steep well provides a large prefactor in the dynamically induced term, and it becomes comparable with instability strength of the bare potential. However, the dynamical stabilization depends on the excited mode: the in-phase mode contributes to stabilize the transition state, while the antiphase mode contributes to enhance the instability, as shown in the previous studies [5,6].

To answer whether the dynamical (de)stabilization has a statistical impact, we compared the reaction rate computed from the transition state theory and from direct MD simulations. The impact of dynamical (de)stabilization is not remarkable. A possible explanation is coexistence of stabilization and destabilization depending on the normal mode energy, which may be thermalized when the system visits a well. Nevertheless, it might be interesting to study whether the small discrepancy between the theory and MD is physically meaningful.

Dynamics of the three-body Lennard-Jones system is considered as the isolated system in this article. It is worth studying DIC with thermal noises, since they are not avoidable in a real system. The essence of DIC is separation of scales in time and space, and, hence, we may expect emergence of DIC even under thermal noises. Another extension of the present theory is a control of molecules by applying an external force and by using the effective local minimum around the transition state. Such a study may give a hint to solve the excited mode dependence of isomer population [25,26].

ACKNOWLEDGMENTS

The author thanks Y. Shimizu for private communications which informed the existence of a stabilized transition state. This work is inspired by these communications. The author acknowledges the support of JSPS KAKENHI Grant No. JP21K03402.

APPENDIX A: THE MATRIX \mathbf{B} AND THE INVERSE MATRIX

In this section, we use the symbol $\mathbf{y} = (l_1, l_2, \phi, \phi_L)$ for the internal coordinates. The matrix $\mathbf{B}(\mathbf{y})$ is of 4×4 accordingly.

We divide the matrix $\mathbf{B}(\mathbf{y})$ into 2×2 matrices as

$$\mathbf{B}(\mathbf{y}) = \begin{pmatrix} \mathbf{B}_{ll}(\mathbf{y}) & \mathbf{B}_{l\phi}(\mathbf{y}) \\ \mathbf{B}_{\phi l}(\mathbf{y}) & \mathbf{B}_{\phi\phi}(\mathbf{y}) \end{pmatrix}, \quad (\text{A1})$$

where

$$\mathbf{B}_{ll}(\mathbf{y}) = \frac{m}{3} \begin{pmatrix} 2 & \cos \phi \\ \cos \phi & 2 \end{pmatrix},$$

$$\mathbf{B}_{l\phi}(\mathbf{y}) = \frac{m}{3} \begin{pmatrix} -\frac{1}{2}l_2 \sin \phi & -l_2 \sin \phi \\ -\frac{1}{2}l_1 \sin \phi & l_1 \sin \phi \end{pmatrix},$$

$$\mathbf{B}_{\phi l}(\mathbf{y}) = \mathbf{B}_{l\phi}(\mathbf{y})^T,$$

$$\mathbf{B}_{\phi\phi}(\mathbf{y}) = \frac{m}{3} \begin{pmatrix} \frac{1}{2}(l_1^2 + l_2^2 - l_1 l_2 \cos \phi) & l_2^2 - l_1^2 \\ l_2^2 - l_1^2 & 2(l_1^2 + l_2^2 + l_1 l_2 \cos \phi) \end{pmatrix}. \quad (\text{A2})$$

The inverse matrix of $\mathbf{B}(\mathbf{y})$ is

$$[\mathbf{B}(\mathbf{y})]^{-1} = \begin{pmatrix} \tilde{\mathbf{B}}_{ll} & \tilde{\mathbf{B}}_{l\phi} \\ \tilde{\mathbf{B}}_{\phi l} & \tilde{\mathbf{B}}_{\phi\phi} \end{pmatrix}, \quad (\text{A3})$$

where

$$\tilde{\mathbf{B}}_{ll}(\mathbf{y}) = \frac{1}{m} \begin{pmatrix} 2 & -\cos \phi \\ -\cos \phi & 2 \end{pmatrix},$$

$$\tilde{\mathbf{B}}_{l\phi}(\mathbf{y}) = \frac{1}{m} \begin{pmatrix} \frac{1}{l_2} \sin \phi & \frac{1}{2l_2} \sin \phi \\ \frac{1}{l_1} \sin \phi & -\frac{1}{2l_1} \sin \phi \end{pmatrix},$$

$$\tilde{\mathbf{B}}_{\phi l}(\mathbf{y}) = \tilde{\mathbf{B}}_{l\phi}(\mathbf{y})^T,$$

$$\tilde{\mathbf{B}}_{\phi\phi}(\mathbf{y}) = \frac{1}{m} \begin{pmatrix} \frac{2}{l_1^2} + \frac{2}{l_2^2} + \frac{2}{l_1 l_2} \cos \phi & \frac{1}{l_2^2} - \frac{1}{l_1^2} \\ \frac{1}{l_2^2} - \frac{1}{l_1^2} & \frac{2}{2l_1^2} + \frac{1}{2l_2^2} - \frac{1}{2l_1 l_2} \cos \phi \end{pmatrix}. \quad (\text{A4})$$

APPENDIX B: EULER-LAGRANGE EQUATIONS

We use the 4×4 matrix $\mathbf{B}(\mathbf{y})$ introduced in Appendix A. We expand the Euler-Lagrange equations

$$\sum_{\beta=1}^4 B^{\alpha\beta} \ddot{y}_\beta + \sum_{\beta,\gamma=1}^4 D^{\alpha\beta\gamma} \dot{y}_\beta \dot{y}_\gamma + \frac{\partial V}{\partial y_\alpha} = 0, \quad \alpha = 1, 2, 3, 4, \quad (\text{B1})$$

associated with the Lagrangian (9) into a power series of the small parameter ϵ . Here,

$$D^{\alpha\beta\gamma}(\mathbf{y}) = \frac{\partial B^{\alpha\beta}}{\partial y_\gamma}(\mathbf{y}) - \frac{1}{2} \frac{\partial B^{\beta\gamma}}{\partial y_\alpha}(\mathbf{y}), \quad \alpha, \beta, \gamma = 1, 2, 3, 4. \quad (\text{B2})$$

1. Expansion of the equations

Substituting Eqs. (18), (20), and (21) into Eq. (B1), we have the equations of motion in each order of ϵ :

$$O(\epsilon^0) : \left(\frac{\partial V}{\partial y_\alpha}(\mathbf{y}) \right)^{(0)} = 0, \quad (\text{B3a})$$

$$O(\epsilon^1) : \sum_{\beta=1}^4 B^{\alpha\beta}(\mathbf{y}^{(0)}) \frac{\partial^2 y_\beta^{(1)}}{\partial t_0^2} + \left(\frac{\partial V}{\partial y_\alpha}(\mathbf{y}) \right)^{(1)} = 0, \quad (\text{B3b})$$

$$O(\epsilon^2) : \sum_{\beta=1}^4 B^{\alpha\beta}(\mathbf{y}^{(0)}) (\ddot{y}_\beta)^{(2)} + \sum_{\beta,\gamma=1}^4 D^{\alpha\beta\gamma}(\mathbf{y}^{(0)}) (\dot{y}_\beta)^{(1)} (\dot{y}_\gamma)^{(1)} + \left(\frac{\partial V}{\partial y_\alpha}(\mathbf{y}) \right)^{(2)} + \sum_{\beta,\gamma=1}^4 \frac{\partial B^{\alpha\beta}}{\partial y_\gamma}(\mathbf{y}^{(0)}) \frac{\partial^2 y_\beta^{(1)}}{\partial t_0^2} y_\gamma^{(1)} = 0, \quad (\text{B3c})$$

where

$$\begin{aligned} (\dot{y}_\beta)^{(1)} &= \frac{dy_\beta^{(0)}}{dt_1} + \frac{\partial y_\beta^{(1)}}{\partial t_0}, \\ (\ddot{y}_\beta)^{(2)} &= \frac{d^2 y_\beta^{(0)}}{dt_1^2} + 2 \frac{\partial^2 y_\beta^{(1)}}{\partial t_0 \partial t_1}. \end{aligned} \quad (\text{B4})$$

The equations in $O(\epsilon^0)$ are satisfied by Eq. (21).

2. Equation in $O(\epsilon)$

The equations of motion in $O(\epsilon)$, Eq. (B3b), are linear and are rewritten as

$$\mathbf{B}^{(0)} \frac{\partial^2 \mathbf{y}^{(1)}}{\partial t_0^2} + \mathbf{K} \mathbf{y}^{(1)} = 0, \quad (\text{B5})$$

where

$$\mathbf{B}^{(0)} = \mathbf{B}(\mathbf{y}^{(0)}) = \frac{m}{3} \begin{pmatrix} 2 & \cos \phi^{(0)} & -\frac{1}{2}l^\ddagger \sin \phi^{(0)} & -l^\ddagger \sin \phi^{(0)} \\ \cos \phi^{(0)} & 2 & -\frac{1}{2}l^\ddagger \sin \phi^{(0)} & l^\ddagger \sin \phi^{(0)} \\ -\frac{1}{2}l^\ddagger \sin \phi^{(0)} & -\frac{1}{2}l^\ddagger \sin \phi^{(0)} & \frac{1}{2}(l^\ddagger)^2(2 - \cos \phi^{(0)}) & 0 \\ -l^\ddagger \sin \phi^{(0)} & l^\ddagger \sin \phi^{(0)} & 0 & 2(l^\ddagger)^2(2 + \cos \phi^{(0)}) \end{pmatrix}, \quad (\text{B6})$$

and

$$\mathbf{K} = U''_{\text{LJ}}(l^\ddagger) \begin{pmatrix} \mathbf{E} & \mathbf{O} \\ \mathbf{O} & \mathbf{O} \end{pmatrix}. \quad (\text{B7})$$

Here, \mathbf{E} represents the unit matrix and \mathbf{O} represents the zero matrix. Substituting $\mathbf{y}^{(1)} = \mathbf{v} \cos(\sqrt{\lambda} t_0)$ into Eq. (B5), we consider the eigenvalue problem

$$(\mathbf{B}^{(0)}\lambda - \mathbf{K})\mathbf{v} = \mathbf{0}, \quad (\text{B8})$$

which induces $\det(\mathbf{B}^{(0)}\lambda - \mathbf{K}) = 0$ to determine λ . We have four sets of λ_i and \mathbf{v}_i ($i = 1, \dots, 4$). Arranging λ_i into a diagonal matrix

$$\mathbf{\Lambda} = \frac{U''_{\text{LJ}}(l^\ddagger)}{m} \text{diag}(2 - \cos \phi^{(0)}, 2 + \cos \phi^{(0)}, 0, 0) \quad (\text{B9})$$

$$\mathbf{\Lambda}_B = \frac{m}{3} \text{diag}\left(\frac{6}{2 - \cos \phi^{(0)}}, \frac{6}{2 + \cos \phi^{(0)}}, \frac{1}{2}(l^\ddagger)^2(2 - \cos \phi^{(0)}), \frac{1}{2}(l^\ddagger)^2(2 + \cos \phi^{(0)})\right). \quad (\text{B12})$$

Therefore, the matrix $\mathbf{P}^T \mathbf{K} \mathbf{P} = \mathbf{P}^T \mathbf{B}^{(0)} \mathbf{P} \mathbf{\Lambda} = \mathbf{\Lambda}_B \mathbf{\Lambda}$ is also diagonal. Performing the change of variables by

$$\mathbf{y}^{(1)} = \mathbf{P} \boldsymbol{\eta}, \quad (\text{B13})$$

the linear equations (B5) are modified into a diagonalized form

$$\frac{\partial^2 \boldsymbol{\eta}}{\partial t_0^2} = -\mathbf{\Lambda} \boldsymbol{\eta}, \quad (\text{B14})$$

where we used the fact $\det \mathbf{\Lambda}_B \neq 0$.

The first two eigenvalues of $\mathbf{\Lambda}$ are positive since $U''_{\text{LJ}}(l^\ddagger) > 0$, and we have two vibrating modes: the in-phase mode (mode-I) and the antiphase mode (mode-II). Let us compute energy for each mode. The linear equations (B5) are derived from the Lagrangian

$$\begin{aligned} L^{(1)} &= \frac{1}{2} \left(\frac{\partial \mathbf{y}^{(1)}}{\partial t_0} \right)^T \mathbf{B}^{(0)} \frac{\partial \mathbf{y}^{(1)}}{\partial t_0} - \frac{1}{2} (\mathbf{y}^{(1)})^T \mathbf{K} \mathbf{y}^{(1)} \\ &= \frac{1}{2} \left(\frac{\partial \boldsymbol{\eta}}{\partial t_0} \right)^T \mathbf{\Lambda}_B \frac{\partial \boldsymbol{\eta}}{\partial t_0} - \frac{1}{2} \boldsymbol{\eta}^T \mathbf{\Lambda}_B \mathbf{\Lambda} \boldsymbol{\eta}. \end{aligned} \quad (\text{B15})$$

Recalling that the amplitudes of the normal modes are of $O(\epsilon)$, we have the normal mode energy of $O(\epsilon^2)$. Energy of the mode-I is hence

$$\frac{E_I}{\epsilon^2} = \frac{m}{2 - \cos \phi^{(0)}} \left(\frac{\partial \eta_1}{\partial t_0} \right)^2 + U''_{\text{LJ}}(l^\ddagger) \eta_1^2 \quad (\text{B16})$$

and of the mode-II is

$$\frac{E_{II}}{\epsilon^2} = \frac{m}{2 + \cos \phi^{(0)}} \left(\frac{\partial \eta_2}{\partial t_0} \right)^2 + U''_{\text{LJ}}(l^\ddagger) \eta_2^2. \quad (\text{B17})$$

and \mathbf{v}_i into a matrix

$$\mathbf{P} = (\mathbf{v}_1, \dots, \mathbf{v}_4) = \begin{pmatrix} 1 & -1 & 0 & 0 \\ 1 & 1 & 0 & 0 \\ \frac{2}{l^\ddagger} \frac{\sin \phi^{(0)}}{2 - \cos \phi^{(0)}} & 0 & 1 & 0 \\ 0 & -\frac{1}{l^\ddagger} \frac{\sin \phi^{(0)}}{2 + \cos \phi^{(0)}} & 0 & 1 \end{pmatrix}, \quad (\text{B10})$$

we have the equality

$$\mathbf{B}^{(0)} \mathbf{P} \mathbf{\Lambda} - \mathbf{K} \mathbf{P} = \mathbf{O}. \quad (\text{B11})$$

We can also show that $\mathbf{P}^T \mathbf{B}^{(0)} \mathbf{P} = \mathbf{\Lambda}_B$ is diagonal, where

Coming back to the coordinate $\mathbf{y}^{(1)}$ by $\boldsymbol{\eta} = \mathbf{P}^{-1} \mathbf{y}^{(1)}$ with

$$\mathbf{P}^{-1} = \begin{pmatrix} 1/2 & 1/2 & 0 & 0 \\ -1/2 & 1/2 & 0 & 0 \\ -\frac{1}{l^\ddagger} \frac{\sin \phi^{(0)}}{2 - \cos \phi^{(0)}} & -\frac{1}{l^\ddagger} \frac{\sin \phi^{(0)}}{2 - \cos \phi^{(0)}} & 1 & 0 \\ -\frac{1}{2l^\ddagger} \frac{\sin \phi^{(0)}}{2 + \cos \phi^{(0)}} & \frac{1}{l^\ddagger} \frac{\sin \phi^{(0)}}{2 + \cos \phi^{(0)}} & 0 & 1 \end{pmatrix}, \quad (\text{B18})$$

we have

$$\frac{E_I}{\epsilon^2} = \frac{m [\partial_{t_0} (l_1^{(1)} + l_2^{(1)})]^2}{4(2 - \cos \phi^{(0)})} + \frac{U''_{\text{LJ}}(l^\ddagger)}{4} (l_1^{(1)} + l_2^{(1)})^2 \quad (\text{B19})$$

and

$$\frac{E_{II}}{\epsilon^2} = \frac{m [\partial_{t_0} (l_1^{(1)} - l_2^{(1)})]^2}{4(2 + \cos \phi^{(0)})} + \frac{U''_{\text{LJ}}(l^\ddagger)}{4} (l_1^{(1)} - l_2^{(1)})^2. \quad (\text{B20})$$

For the initial condition discussed in Sec. V A, the initial values of E_I and E_{II} result in Eq. (25), since $\delta l_i = \epsilon l_i^{(1)}$.

3. Equation in $O(\epsilon^2)$

Taking the average over the fast timescale t_0 , we have in $O(\epsilon^2)$

$$\begin{aligned} & \sum_{\beta=1}^4 B^{\alpha\beta} \frac{d^2 y_\beta^{(0)}}{dt_1^2} + \sum_{\beta, \gamma=1}^4 D^{\alpha\beta\gamma} \frac{dy_\beta^{(0)}}{dt_1} \frac{dy_\gamma^{(0)}}{dt_1} \\ &= - \left\langle \left(\frac{\partial V}{\partial y_\alpha} \right)^{(2)} \right\rangle - \frac{1}{2} \sum_{\beta, \gamma=1}^4 \frac{\partial B^{\beta\gamma}}{\partial y_\alpha} \left\langle y_\beta^{(1)} \frac{\partial^2 y_\gamma^{(1)}}{\partial t_0^2} \right\rangle, \end{aligned} \quad (\text{B21})$$

where $B^{\alpha\beta}$, $D^{\alpha\beta\gamma}$, and $\partial B^{\beta\gamma} / \partial y_\alpha$ are evaluated at $\mathbf{y} = \mathbf{y}^{(0)}$. The symbol $\langle \dots \rangle$ represents the average over t_0 . The left-hand side comes from the leading-order geodesic equation in

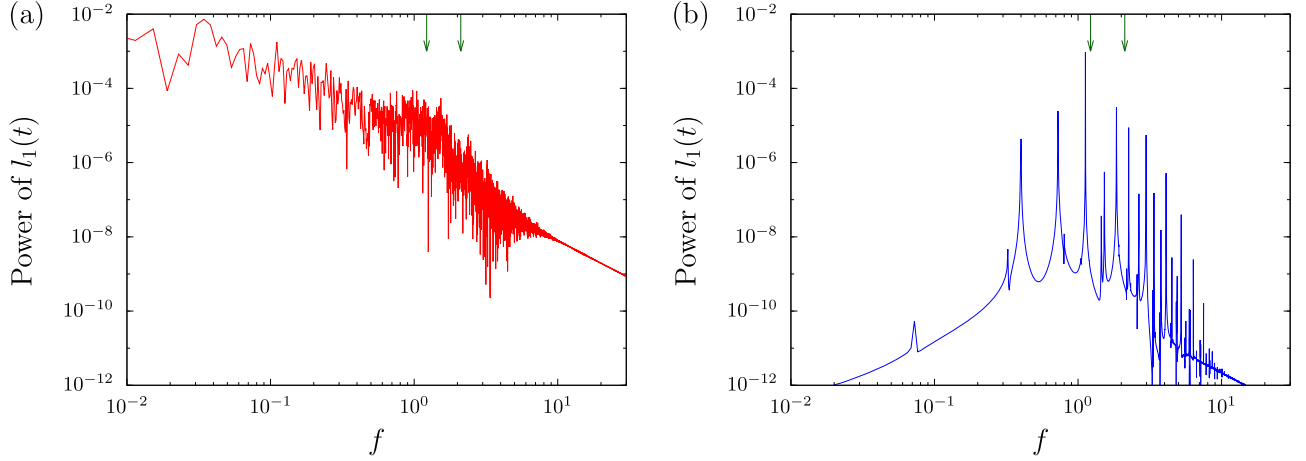


FIG. 10. Power spectra of $l_1(t)$. (a) Corresponding to the time series of Fig. 5(a). (b) Corresponding to the time series of Fig. 5(b). The small down arrows mark from left to right the eigenfrequencies of the in-phase and antiphase modes, respectively, which are defined in $O(\epsilon)$ at $\phi = 0$ (straight conformation).

the metric space with $\mathbf{B}(\mathbf{y})$ [see Eq. (B1)], the first term of the right-hand side is the averaged bare potential force, and the second term is the additional effective force, which is obtained by performing the integration by parts.

From now on, we focus on the equation of motion for ϕ , i.e., $\alpha = 3$ in Eq. (B21). Around $\mathbf{y} = \mathbf{y}^\ddagger$, the averaged bare potential force is

$$-\left\langle \left(\frac{\partial V}{\partial \phi} \right)^{(2)} \right\rangle = -\frac{1}{\epsilon^2} \frac{\partial V}{\partial \phi} (l^\ddagger, l^\ddagger, \phi^{(0)}), \quad (\text{B22})$$

which is of $O(\epsilon^0)$. From (B5), the second term denoted by A is modified into

$$A = \frac{1}{2} \text{Tr} \left[\mathbf{P}^T \frac{\partial \mathbf{B}}{\partial \phi} \mathbf{P} \Lambda \langle \eta \eta^T \rangle \right], \quad (\text{B23})$$

where Tr represents trace. For $\boldsymbol{\eta} = (\eta_1, \eta_2, \eta_3, \eta_4)$ we have

$$\Lambda \langle \eta \eta^T \rangle = \frac{U_{\text{LJ}}''(l^\ddagger)}{m} \text{diag}((2 - \cos \phi^{(0)}) \langle \eta_1^2 \rangle, (2 + \cos \phi^{(0)}) \langle \eta_2^2 \rangle, 0, 0). \quad (\text{B24})$$

This form implies that, to obtain A , we need only the first two diagonal elements of $\mathbf{P}^T (\partial \mathbf{B} / \partial \phi) \mathbf{P}$, which is read as

$$\mathbf{P}^T \frac{\partial \mathbf{B}}{\partial \phi} \mathbf{P} = \begin{pmatrix} \begin{pmatrix} \frac{-2m \sin \phi^{(0)}}{[2 - \cos \phi^{(0)}]^2} & 0 \\ 0 & \frac{2m \sin \phi^{(0)}}{[2 + \cos \phi^{(0)}]^2} \end{pmatrix} & * \\ * & * \end{pmatrix}. \quad (\text{B25})$$

The factor A is hence

$$A = -U_{\text{LJ}}''(l^\ddagger) \left(\frac{\sin \phi^{(0)}}{2 - \cos \phi^{(0)}} \langle \eta_1^2 \rangle - \frac{\sin \phi^{(0)}}{2 + \cos \phi^{(0)}} \langle \eta_2^2 \rangle \right). \quad (\text{B26})$$

For the normal modes described by Eqs. (B16) and (B17), the averages of amplitudes are, respectively,

$$\langle \eta_1^2 \rangle = \frac{E_I}{2\epsilon^2 U_{\text{LJ}}''(l^\ddagger)}, \quad \langle \eta_2^2 \rangle = \frac{E_{\text{II}}}{2\epsilon^2 U_{\text{LJ}}''(l^\ddagger)}. \quad (\text{B27})$$

Finally, from the relations

$$E_I = E_{\text{normal}} \nu_I, \quad E_{\text{II}} = E_{\text{normal}} \nu_{\text{II}}, \quad (\text{B28})$$

we have

$$A = -\frac{E_{\text{normal}}}{2\epsilon^2} \sin \phi^{(0)} \left(\frac{\nu_I}{2 - \cos \phi^{(0)}} - \frac{\nu_{\text{II}}}{2 + \cos \phi^{(0)}} \right). \quad (\text{B29})$$

This additional term gives the effective force (26).

APPENDIX C: POWER SPECTRA OF $l_1(t)$

We report in Fig. 10 power spectra of $l_1(t)$, which correspond to the time series of Figs. 5(a) and 5(b). We select $l_1(t)$ instead of $l_3(t)$, since l_3 is almost dominated by the in-phase mode around a straight conformation. We pick up a period of $2^{18} \Delta t$, where $\Delta t = 10^{-3}$ is the timestep of molecular dynamics. A nonstabilized saddle experiences chaotic dynamics by visiting bottoms of potential landscape, and the power spectrum is broad [Fig. 10(a)]. Around a stabilized saddle, the power spectrum has sharp peaks and motion is regular [Fig. 10(b)].

The above difference is also observed in two time regions of the orbit shown in Fig. 5(c); The saddle point keeps (loses) stability in the time region $t < 600$ ($t > 650$). In each of the time regions, we pick up a time sequence of $l_1(t)$ in a period of $2^{18} \Delta t$. The power spectrum in the stabilized time region is reported in Fig. 11(a), and it has peaks as Fig. 10(b), although the peaks are shifted and fade due to stronger nonlinear effects. After losing the stability, the power spectrum reported in Fig. 11(b) is broad as Fig. 10(a).

APPENDIX D: HAMILTONIAN FORMALISM OF THE SYSTEM

The Hamiltonian of the system is expressed by

$$H(\mathbf{y}, \mathbf{p}) = \frac{1}{2} \sum_{\alpha, \beta=1}^4 \tilde{B}_{\alpha\beta}(\mathbf{y}) p^\alpha p^\beta + V(\mathbf{y}), \quad (\text{D1})$$

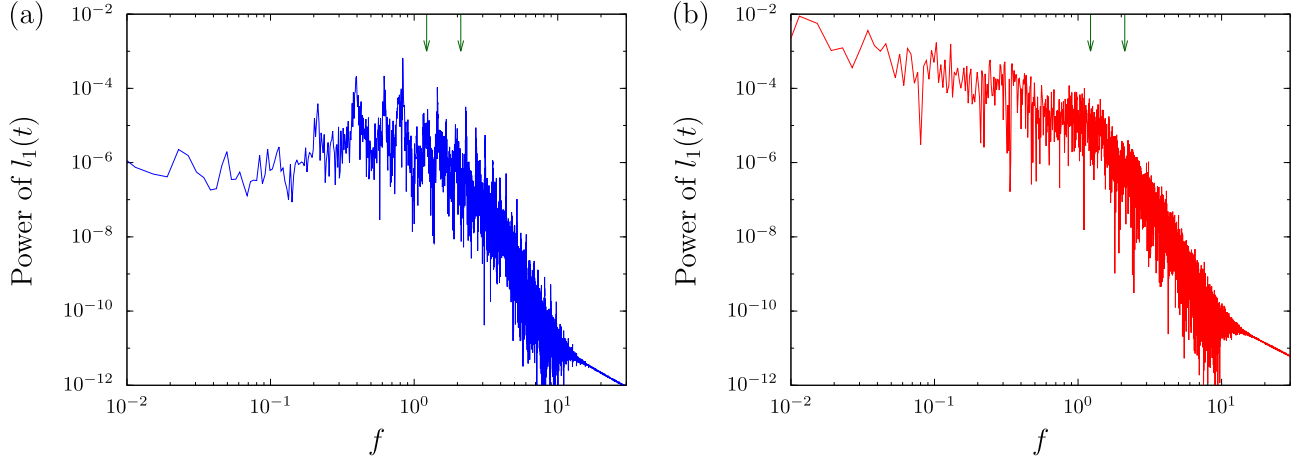


FIG. 11. Power spectra of $l_1(t)$ corresponding to Fig. 5(c). (a) Stable time region $t < 600$. (b) After losing the stability $t > 650$. The small down arrows mark from left to right the eigenfrequencies of the in-phase and antiphase modes respectively, which are defined in $O(\epsilon)$ at $\phi = 0$ (straight conformation).

where $\tilde{B}_{\alpha\beta}(\mathbf{y})$ is the (α, β) element of the inverse matrix of $\mathbf{B}(\mathbf{y})$ [see Eq. (A4)]. The transformations between the momentum vector $\mathbf{p} = (p^1, p^2, p^3, p^4)$ and the velocity vector $\dot{\mathbf{y}} = (\dot{y}_1, \dot{y}_2, \dot{y}_3, \dot{y}_4) = (\dot{l}_1, \dot{l}_2, \dot{\phi}, \dot{\phi}_L)$ are

$$p^\alpha = \sum_{\beta=1}^4 B^{\alpha\beta}(\mathbf{y}) \dot{y}_\beta, \quad \dot{y}_\alpha = \sum_{\beta=1}^4 \tilde{B}_{\alpha\beta}(\mathbf{y}) p^\beta. \quad (\text{D2})$$

The inverse matrix $[\mathbf{B}(\mathbf{y})]^{-1}$ gives the velocity $\dot{\phi}$ as

$$\dot{\phi} = \frac{1}{m} \left[2p^3 \left(\frac{1}{l_1^2} + \frac{1}{l_2^2} + \frac{1}{l_1 l_2} \cos \phi \right) + \left(\frac{p^1}{l_2} + \frac{p^2}{l_1} \right) \sin \phi \right] \quad (\text{D3})$$

for the vanishing total angular momentum, $p^4 \equiv 0$. Similarly, the sum in the kinetic term runs from 1 to 3 in the Hamiltonian (D1).

-
- [1] A. Stephenson, XX. On induced stability, *The London, Edinburgh, and Dublin, Philosophical Magazine and Journal of Science* **15**, 233 (1908).
 - [2] P. L. Kapitza, Dynamic stability of a pendulum when its point of suspension vibrates, *Sov. Phys. JETP* **21**, 588 (1951); Collected papers of Vol. 2, pp. 714–737 (1965).
 - [3] E. I. Butikov, On the dynamic stabilization of an inverted pendulum, *Am. J. Phys.* **69**, 755 (2001).
 - [4] M. Bukov, L. D'Alessio, and A. Polkovnikov, Universal high-frequency behavior of periodically driven systems: from dynamical stabilization to Floquet engineering, *Adv. Phys.* **64**, 139 (2015).
 - [5] Y. Y. Yamaguchi, T. Yanagita, T. Konishi, and M. Toda, Dynamically induced conformation depending on excited normal modes of fast oscillation, *Phys. Rev. E* **105**, 064201 (2022).
 - [6] Y. Y. Yamaguchi, Mode selectivity of dynamically induced conformation in many-body chainlike bead-spring models, *Phys. Rev. E* **107**, 064212 (2023).
 - [7] P. E. Rouse, Jr., A theory of the linear viscoelastic properties of dilute solutions of coiling polymers, *J. Chem. Phys.* **21**, 1272 (1953).
 - [8] T. Yanagita and T. Konishi, Numerical analysis of new oscillatory mode of bead-spring model, *J. JSCE* **75**, 1_125 (2019).
 - [9] C. M. Bender and S. A. Orszag, *Advanced Mathematical Methods for Scientists and Engineers I: Asymptotic Methods and Perturbation Theory* (Springer, New York, 1999).
 - [10] N. M. Krylov and N. N. Bogoliubov, *New Methods of Nonlinear Mechanics in their Application to the Investigation of the Operation of Electronic Generators. I* (United Scientific and Technical Press, Moscow, 1934).
 - [11] N. M. Krylov and N. N. Bogoliubov, *Introduction to Nonlinear Mechanics* (Princeton University Press, Princeton, 1947).
 - [12] J. Guckenheimer and P. Holmes, *Nonlinear Oscillations, Dynamical Systems, and Bifurcations of Vector Fields* (Springer-Verlag, New York, 1983).
 - [13] J. E. Lennard-Jones, Cohesion, *Proc. Phys. Soc.* **43**, 461 (1931).
 - [14] J. Fischer and M. Mendland, On the history of key empirical intermolecular potentials, *Fluid Phase Equilib.* **573**, 113876 (2023).
 - [15] J. Lenhard, S. Stephan, and H. Hasse, On the history of the Lennard-Jones Potential, *Ann. Phys.* **536**, 2400115 (2024).
 - [16] Y. Shimizu (private communications).
 - [17] R. A. Marcus and O. K. Rice, The kinetics of the recombination of methyl radicals and iodine atoms, *J. Phys. Chem.* **55**, 894 (1951).
 - [18] R. A. Marcus, Unimolecular dissociation and free radical recombination reactions, *J. Chem. Phys.* **20**, 359 (1952).
 - [19] H. M. Rosenstock, M. B. Wallenstein, A. L. Wahrhaftig, and H. Eyring, Absolute rate theory for isolated systems and the mass spectra of polyatomic molecules, *Proc. Natl. Acad. Sci. USA* **38**, 667 (1952).
 - [20] J. L. Magee, Theory of the chemical reaction rate constant, *Proc. Natl. Acad. Sci. USA* **38**, 764 (1952).

- [21] J. C. Giddings and H. Eyring, Equilibrium theory of unimolecular reactions, *J. Chem. Phys.* **22**, 538 (1954).
- [22] G. M. Wieder and R. A. Marcus, Dissociation and isomerization of vibrationally excited species. II. Unimolecular reaction rate theory and its application, *J. Chem. Phys.* **37**, 1835 (1962).
- [23] K. J. Laidler and M. C. King, Development of transition-state theory, *J. Phys. Chem.* **87**, 2657 (1983).
- [24] D. G. Truhlar, B. C. Garrett, and S. J. Klippenstein, *J. Phys. Chem.* **100**, 12771 (1996).
- [25] B. C. Dian, A. Longarte, and T. S. Zwier, Conformational dynamics in a dipeptide after single-mode vibrational excitation, *Science* **296**, 2369 (2002).
- [26] B. C. Dian, A. Longarte, P. R. Winter, and T. S. Zwier, The dynamics of conformational isomerization in flexible biomolecules. I. Hole-filling spectroscopy of N-acetyl tryptophan methyl amide and N-acetyl tryptophan amide, *J. Chem. Phys.* **120**, 133 (2004).
- [27] T. Yanao and K. Takatsuka, Collective coordinates and an accompanying metric force in structural isomerization dynamics of molecules, *Phys. Rev. A* **68**, 032714 (2003).
- [28] T. Yanao and K. Takatsuka, Kinematic effects associated with molecular frames in structural isomerization dynamics of clusters, *J. Chem. Phys.* **120**, 8924 (2004).
- [29] T. Yanao and K. Takatsuka, Effects of an intrinsic metric of molecular internal space on chemical reaction dynamics, in *Geometric Structures of Phase Space in Multi-Dimensional Chaos: Applications to Chemical Reaction Dynamics in Complex Systems*, edited by M. Toda, T. Komatsuzaki, T. Konishi, and R. S. Berry, Advanced in Chemical Physics, Vol. 130 (John Wiley & Sons, New Jersey, 2005), Chap. 12.
- [30] T. Yanao, W. S. Koon, J. E. Marsden, and I. G. Kevrekidis, Gyration-radius dynamics in structural transitions of atomic clusters, *J. Chem. Phys.* **126**, 124102 (2007).
- [31] H. Yoshida, Construction of higher order symplectic integrators, *Phys. Lett. A* **150**, 262 (1990).